

See discussions, stats, and author profiles for this publication at: <https://www.researchgate.net/publication/228443337>

Total variation regularization for bioluminescence tomography with the split Bregman method

Article in *Applied Optics* · July 2012

DOI: 10.1364/AO.51.004501 · Source: PubMed

CITATIONS

14

READS

38

9 authors, including:



Shuping Zhu

Xidian University

49 PUBLICATIONS 629 CITATIONS

SEE PROFILE



Kai Liu

the ninth hospital Shanghai Jiao Tong Unive...

76 PUBLICATIONS 624 CITATIONS

SEE PROFILE



Xin Yang

Chinese Academy of Sciences

132 PUBLICATIONS 1,137 CITATIONS

SEE PROFILE



Jie Tian

Chinese Academy of Sciences

661 PUBLICATIONS 7,099 CITATIONS

SEE PROFILE

All content following this page was uploaded by **Jie Tian** on 12 October 2015.

The user has requested enhancement of the downloaded file. All in-text references underlined in blue are linked to publications on ResearchGate, letting you access and read them immediately.

Total variation regularization for bioluminescence tomography with the split Bregman method

Jinchao Feng,^{1,†} Chenghu Qin,^{2,†} Kebin Jia,^{1,*} Shouping Zhu,³ Kai Liu,² Dong Han,²
Xin Yang,² Quansheng Gao,³ and Jie Tian^{2,4,5}

¹College of Electronic Information & Control Engineering, Beijing University of Technology, Beijing 100124, China

²Intelligent Medical Research Center, Institute of Automation, Chinese Academy of Sciences, Beijing 100190, China

³Laboratory Animal Center, Academy of Military Medical Sciences, Beijing 100850, China

⁴Life Science Research Center, Xidian University, Xi'an 710071, China

⁵e-mail: tian@ieee.org

*Corresponding author: kebinj@bjut.edu.cn

Received 28 July 2011; revised 10 May 2012; accepted 17 May 2012;
posted 18 May 2012 (Doc. ID 151779); published 29 June 2012

Regularization methods have been broadly applied to bioluminescence tomography (BLT) to obtain stable solutions, including l_2 and l_1 regularizations. However, l_2 regularization can oversmooth reconstructed images and l_1 regularization may sparsify the source distribution, which degrades image quality. In this paper, the use of total variation (TV) regularization in BLT is investigated. Since a nonnegativity constraint can lead to improved image quality, the nonnegative constraint should be considered in BLT. However, TV regularization with a nonnegativity constraint is extremely difficult to solve due to its nondifferentiability and nonlinearity. The aim of this work is to validate the split Bregman method to minimize the TV regularization problem with a nonnegativity constraint for BLT. The performance of split Bregman-resolved TV (SBRTV) based BLT reconstruction algorithm was verified with numerical and *in vivo* experiments. Experimental results demonstrate that the SBRTV regularization can provide better regularization quality over l_2 and l_1 regularizations. © 2012 Optical Society of America

OCIS codes: 170.3010, 170.6280, 170.6960.

1. Introduction

The application of bioluminescence imaging in small animal studies has become more and more attractive in drug development over the recent years because it has the ability to noninvasively screen, analyze, and monitor the animal subjects before, during, and after the experimental intervention or drug administration producing quantitative surrogate measurements of study outcomes [1–3]. In addition, high detection sensitivities can be achieved in bioluminescence imaging due to low background light and the absence of autofluorescence [4]. Therefore, bioluminescence

imaging is a particularly elegant imaging technique for *in vivo* imaging of the whole body of a small animal. Although encouraging, many of these earlier studies utilized planar imaging techniques, which were incapable of providing depth information of the source. Therefore, recent advances have focused on improving instrumentation and algorithms to allow tomography imaging, which facilitates the emergence of bioluminescence tomography (BLT) [5].

As a new tomographic technique, BLT has obtained much attention. The objective of BLT is to find the unknown bioluminescent source distribution inside tissue from the noisy measurements on the tissue surface. However, due to strong light scattering and the limited boundary measurement data, the inverse problem of BLT is ill-posed and underdetermined.

The ill-posedness makes the BLT reconstruction sensitive to small perturbation in the measurement data, such as noise. Therefore, to obtain reasonable reconstructions, a sequence of reconstruction algorithms based on the regularization technique are developed [6–14].

However, despite these advances, BLT is not yet widely used. One of the major barriers to widespread acceptance is that reconstructed images have a poor quality. Among the current BLT reconstruction algorithms, the popular algorithm is used to adopt the Tikhonov regularization, which inherently provides smoothed solutions and therefore offers compromised accuracy in localizing bioluminescent sources. Recently, sparsity-inducing (usually l_1) regularized problems have received an increasing amount of attention in optical imaging, which allow high quality images to be reconstructed from a small amount of measurements [6,7]. However, l_1 regularized problems may sparsify the bioluminescent source distribution, which degrades the image quality [7].

Total variation (TV) regularization was first introduced in [15]. To date, TV regularization has widespread applications for various aspects in image processing and image reconstruction, such as image denoising [16], blind deconvolution [17], diffuse optical tomography (DOT) [18], and photoacoustic tomography (PAT) [19,20]. In [18–20], a total variation minimization (TVM) based reconstruction algorithm is applied in DOT and PAT based on the finite element method (FEM) scheme, which is much easier to implement and requires much fewer modifications to the existing algorithms. The algorithm is not time-consuming compared to other regularizations, and does not require large amounts of computer memory. Their results have been confirmed and evaluated using phantom experiments. However, the TVM based reconstruction algorithm is an unconstrained algorithm. Therefore, it cannot be directly used for BLT because constrains on the bioluminescent source are generally taken into account in the inversion reconstruction [6,7,21–23].

For BLT experiments, the bioluminescent source density is generally assumed to be stable when photons are collected [13]; therefore, the source distribution can be taken as a nearly piecewise-constant. Furthermore, TV regularization is effective for piecewise-constant reconstruction [15]. As a result, TV regularization is a particularly attractive and natural choice for inverse reconstruction of piecewise-constant source distribution in BLT. However, TV regularization is one of the most difficult optimizations to be solved computationally because of the nonsmooth and nondifferentiable properties of the TV regularizer, which prevents TV regularization from the application in BLT. Recently, TV regularization for BLT has been studied in [7], where a novel interior-point algorithm is proposed for solving the TV regularization that uses the preconditioned conjugate gradient algorithm to compute the search direction. Although this method is successful for BLT

reconstructions, the nonnegativity constraint that has been proven to be very helpful to improve BLT reconstruction results is not considered [23]. Therefore, it is desirable to develop the algorithm that is capable of solving the TV regularization with the nonnegativity constraint effectively. Moreover, it should be noted that only two-dimensional (2D) numerical simulations were performed to evaluate their algorithm in [7]. The performance of TV regularization in BLT still needs to be explored thoroughly.

In this paper, we studied the TV regularization based reconstruction algorithm for BLT. Considering the computational complexity of TV regularization with the nonnegativity constraint, the split Bregman method was applied to solve the TV regularization based BLT reconstruction algorithm. Its idea is to introduce an auxiliary variable to decompose a complex optimization problem into two independent suboptimization problems, which are simple to implement. It is the synergistic combination of the split Bregman method and TV regularization in improving the reconstructed image quality of BLT. Moreover, based on the split Bregman method, the existing iterative algorithms can be used in designing a computationally efficient solver of the TV-regularized BLT reconstruction algorithm. Various experiments including 2D, three-dimensional (3D) numerical simulations, and 3D *in vivo* experiments were performed to fully evaluate the performance of the algorithm. To the best of our knowledge, the split Bregman-resolved TV (SBRTV) regularization based BLT reconstruction algorithm has not been presented in the literature.

The rest of this paper is organized as follows. In Section 2 we briefly review the forward model based on the diffusion equation and introduce the TV regularization. Then we present how we use the split Bregman method to solve it. In Section 3 we present the numerical and *in vivo* results to validate the performance of the SBRTV regularization, and compare it with the l_2 and l_1 regularizations. In Section 4 we will conclude and address open questions.

2. Methods

A. Forward Model

The propagation of light in highly scattering biological tissues is typically modeled by the diffusion equation, which is a first order approximation for the radiative transfer equation. Furthermore, if photons at different wavelengths are considered, the governing mathematical model of BLT can be given by [9,10]

$$-\nabla \cdot (D(\mathbf{r}, \lambda) \nabla \Phi(\mathbf{r}, \lambda)) + \mu_a(\mathbf{r}, \lambda) \Phi(\mathbf{r}, \lambda) = S(\mathbf{r}, \lambda) \quad (\mathbf{r} \in \Omega), \quad (1)$$

$$\Phi(\mathbf{r}, \lambda) + 2A(\mathbf{r}; n, n') D(\mathbf{r}, \lambda) (\nu(\mathbf{r}, \lambda) \cdot \nabla \Phi(\mathbf{r}, \lambda)) = 0 \quad (\mathbf{r} \in \partial\Omega), \quad (2)$$

where $\Omega \in \mathbb{R}^d$, $d = 2, 3$ is the animal volume, $\partial\Omega$ is the animal surface, \mathbf{r} denotes the location vector, $\Phi(\mathbf{r}, \lambda)$ denotes the photon flux density, $\mathbf{S}(\mathbf{r}, \lambda)$ represents the bioluminescent source distribution, λ is the wavelength, and $D(\mathbf{r}, \lambda) = 1/(3(\mu_a(\mathbf{r}, \lambda) + \mu'_s(\mathbf{r}, \lambda)))$, with $\mu_a(\mathbf{r}, \lambda)$ and $\mu'_s(\mathbf{r}, \lambda)$ being the absorption and the reduced scattering coefficients, respectively. $\nu(\mathbf{r})$ is the unit outer normal on $\partial\Omega$. Given the mismatch between the refractive indices n for Ω and n' for the external medium, $A(\mathbf{r}; n, n')$ can be approximately represented as

$$A(\mathbf{r}; n, n') \approx \frac{1 + R(\mathbf{r})}{1 - R(\mathbf{r})}, \quad (3)$$

where n' is close to 1.0 when the mouse is in the air; $R(\mathbf{r})$ can be approximated by $R(\mathbf{r}) \approx -1.4399n^{-2} + 0.7099n^{-1} + 0.6681 + 0.0636n$ [21]. The measured quantity is the outgoing flux density $Q(\mathbf{r}, \lambda)$ on boundary $\partial\Omega$, and it can be expressed as

$$Q(\mathbf{r}, \lambda) = -D(\mathbf{r})(\nu \cdot \nabla \Phi(\mathbf{r}, \lambda)) = \frac{\Phi(\mathbf{r}, \lambda)}{2A(\mathbf{r}; n, n')} (\mathbf{r} \in \partial\Omega). \quad (4)$$

Throughout this presentation, we assume that the coefficients (except for the bioluminescent source S) are known but are different for different tissues.

B. TV Regularization

The aim of BLT is to recover the unknown source distribution S from measurements of the escaped light Φ_{meas} , which amounts to solving the operator equation

$$F(S) = \Phi_{\text{meas}}. \quad (5)$$

The operator F can be obtained by solving the diffusion equation with a FEM over the source spectrum [24]. Because of the ill-posed nature of the inverse problem or the noise in the measurement data, it is impractical to directly solve Eq. (5) [25]. Therefore, it is essential to use regularization methods to obtain the meaningful solutions. Based on regularization methods, the BLT reconstruction is formulated as the following minimization problem:

$$S = \arg \min_{S \geq 0} \|F(S) - \Phi_{\text{meas}}\|_2^2 + \alpha J(S), \quad (6)$$

where $J(S)$ is the regularization term, and $\alpha > 0$ is the regularization parameter, which provides a tradeoff between the data fidelity and the regularization term. By solving the minimization, the distribution of the source can be recovered. The recovered image quality strongly depends on the choice of $J(S)$. In the case of $J(s) = \|s\|_2^2$, i.e., l_2 regularization, the reconstructed image of BLT is usually blurred with a low resolution. When $J(s) = \|s\|_1$, the minimization problem becomes the l_1 regularization, which tends to find sparse solutions. However, the objective function is no longer differentiable, so solving it is a computationally

challenging problem. Moreover, the source distribution may be sparsified. Therefore, we investigated a TV regularization in this paper, which can be defined as [26]

$$J(S) = \|S\|_{\text{TV}} = \int_{\Omega} |\nabla S| d\mathbf{r}, \quad (7)$$

where $\|\cdot\|_{\text{TV}}$ denotes the TV norm. $\|S\|_{\text{TV}}$ can be simply converted to the following matrix form based on the FEM [7], which is

$$\|S\|_{\text{TV}} = |DS|. \quad (8)$$

The difficulty for solving Eq. (8) is that the term $|DS|$ is inseparable. Therefore, one cannot simply use the existing methods.

C. The Split Bregman Method for TV Regularization

The split Bregman method was introduced in [27] as an efficient tool to solve the TV regularization. Its idea is to introduce an auxiliary variable. Based on the split Bregman method, to solve the TV regularization, we first replace $|DS|$ with u . This yields the constrained problem

$$\min_{S \geq 0} \|AS - \Phi_{\text{meas}}\|_2^2 + \lambda \cdot |u| \quad \text{s.t.} \quad DS = u. \quad (9)$$

We can approximate Eq. (9) by adding a penalty function term as done in [28–31] to obtain an unconstrained problem. This yields

$$\min_{S \geq 0} \|AS - \Phi_{\text{meas}}\|_2^2 + \lambda \cdot |u| + \frac{\mu}{2} \|DS - u\|_2^2, \quad (10)$$

where μ is a positive penalization parameter. Finally, we strictly enforced the constraints by applying the Bregman iteration to obtain two subproblems:

$$\begin{aligned} (S_{k+1}, u_{k+1}) &= \min_{S \geq 0, u} \|AS - \Phi_{\text{meas}}\|_2^2 + \lambda \cdot |u| + \frac{\mu}{2} \\ &\quad \cdot \|DS - u - b_k\|_2^2, \\ b_{k+1} &= b_k + u_{k+1} - DS_{k+1}. \end{aligned}$$

In order to further simplify the subproblems, we split the first subproblem into two separate ones, thus obtaining

$$\begin{aligned} \text{Step 1: } S_{k+1} &= \min_{S \geq 0} \|AS - \Phi_{\text{meas}}\|_2^2 + \frac{\mu}{2} \cdot \|DS - u - b_k\|_2^2, \\ \text{Step 2: } u_{k+1} &= \min_u \lambda \cdot |u| + \frac{\mu}{2} \cdot \|DS_{k+1} - u - b_k\|_2^2, \\ \text{Step 3: } b_{k+1} &= b_k + u_{k+1} - DS_{k+1}. \end{aligned} \quad (11)$$

Note that in step 1 we have “decoupled” S from the TV portion of the minimization problem; therefore, S can be solved easily since S is differentiable now. As a result, a wide variety of optimization techniques can be applied to solve the problem. Meanwhile, in step 2,

there is no coupling between elements of u . u can be solved by the fast optimization method. Specifically, the optimal value of u can be computed explicitly using shrinkage operators. That is

$$u_{k+1} = \text{shrink}\left(DS_{k+1} - b_k, \frac{\lambda}{\mu}\right), \quad (12)$$

where

$$\text{shrink}(r, \xi) = \frac{r}{|r|} * \max(|r| - \xi, 0). \quad (13)$$

The implementation of the split Bregman method for TV regularization is formulated as in Algorithm 1.

Algorithm 1: The Split Bregman Method for TV Regularization

Given $\epsilon > 0$, N_{inner} and N_{outer}
1: While $\|S_{k+1} - S_k\| / \|S_{k+1}\| > \epsilon$ and $k < N_{\text{outer}}$
2: For $n = 1$ to N_{inner}
3: $S_{k+1} = \min_{S \geq 0} \|AS - \Phi^{\text{meas}}\|_2^2 + \frac{\mu}{2} \cdot \|DS - u_k - b_k\|_2^2$
4: $u_{k+1} = \min_u \lambda |u| + \frac{\mu}{2} \cdot \|DS_{k+1} - u - b_k\|_2^2$
5: End For
6: $b_{k+1} = b_k + u_{k+1} - DS_{k+1}$
7: End

3. Results

In this section, we used various experiments including simulations and an *in vivo* experiment to validate the SBRTV regularization algorithm. To demonstrate its effectiveness, we compared it with the commonly used l_2 and l_1 regularizations. For numerical simulations, the experiments were mainly performed in 2D, which served the purposes of this paper because the data in 2D was small and required less computational time. In addition, 3D numerical experiments and *in vivo* study were further performed to demonstrate the effectiveness of our algorithm. Note that the regularization parameters used in l_2 and l_1 regularizations in the whole paper were chosen by an adaptive regularization parameter choosing strategy [32]. And the regularization parameters for the SBRTV regularization were selected from a range of regularization parameters based on visual assessment.

A. 2D Results

To demonstrate the effectiveness of the proposed algorithm, numerical simulations were first performed on a 2D circle with a 10 mm radius. Five types of cases were investigated: a domain with a single source (case 1), a nonnegativity constraint (case 2), a domain with multiple sources (case 3), noisy data (case 4), and different numbers of detectors (case 5). For the simulated measurements, two bands (600 and 620 nm) were adopted, and the corresponding optical parameters were summarized in Table 1 [8].

In all of the simulations, the measured data were generated by finite element simulations on a finer mesh. In order to avoid the “inverse crime,” we used

Table 1. Optical Parameters for Different Bands [8]

Wavelength	600 nm	620 nm
μ_a [mm ⁻¹]	0.0281	0.0109
μ'_s [mm ⁻¹]	1.6667	1.6129

FEMs on a coarser mesh consisting of 1309 nodes and 2491 triangular elements with 125 boundary nodes for BLT reconstructions. Since two wavelengths were used in BLT reconstructions, 1309 unknown variables needed to be recovered using 250 boundary measurements. For all reconstructions with the SBRTV regularization, we chose $\mu = \lambda * 10$ unless otherwise noted, which usually resulted in good results. As for the stopping condition, we chose $\|S_{k+1} - S_k\| / \|S_{k+1}\| \leq 4.0 \times 10^{-2}$. Note that the images are shown as what they originally are from reconstructions without further image processing.

1. Case 1: The Influence of the SBRTV Regularization

In the first case, we investigated a situation in which a single bioluminescent source (source 1; see Fig. 1) with a 2 mm diameter was centered at a depth of 5 mm. For comparison, various regularization terms were utilized. We presented the results for l_2 , l_1 , and SBRTV regularizations. For the minimization of the l_2 norm and the optimization subproblem (step 1) of the TV norm, we used a reflective Newton method [33]. For the minimization of the l_1 norm, a gradient projection based method was used [34]. The regularization parameter used in the three regularization algorithms could be found in Table 2. The images from different regularization methods are shown in Fig. 2. We noticed that the reconstructed sources were localized for all methods. However, we can

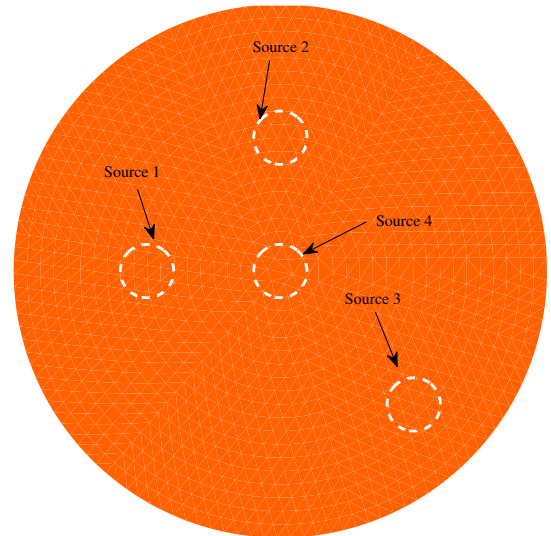


Fig. 1. (Color online) Source configuration of the phantom. There are four sources with a diameter of 2 mm, whose boundary is delineated by the dashed lines. The source densities (unit: nano-Watts/mm²) for sources 1, 2, 3, and 4 were 31, 34, 33, and 36 respectively.

Table 2. Reconstruction Results using l_2 , l_1 , and SBRTV Regularization Methods in Case of Single Source

Regularization method	Regularization parameter	Reconstructed position error	Reconstructed density error	MSE
l_2	2.15×10^{-6}	0.21 mm	77.81%	5.62
l_1	4.91×10^{-5}	0.89 mm	51.52%	6.39
SBRTV	9.9×10^{-8}	0.21 mm	6.67%	4.05

see that the image [Fig. 2(a)] of l_2 reconstruction is slightly oversmoothed. The source distribution of l_1 reconstruction [Fig. 2(b)] is sparsified, and there is a small bias between the reconstructed source and the actual source. Contrary to l_2 and l_1 regularizations, the source is well localized in space, and SBRTV regularization [Fig. 2(c)] yields the best results. Furthermore, the recovered source densities for l_2 , l_1 , and SBRTV are 6.88, 15.03, and 28.90, respectively. The true source density is 31; therefore, SBRTV regularization has a least density loss and a much lower mean squared error (MSE) [34] com-

pared with l_2 and l_1 regularizations. Quantitative results were compiled in Table 2, which illustrated the enhanced quality of reconstructed images with SBRTV regularization.

2. Case 2: Nonnegative Constraint

For BLT reconstruction algorithms, a nonnegativity constraint is generally imposed because the source strength is physically nonnegative. Nevertheless, the nonnegativity constraint adds the computational complexity. In [23], it is illustrated that using a nonnegativity constraint, the performance of the

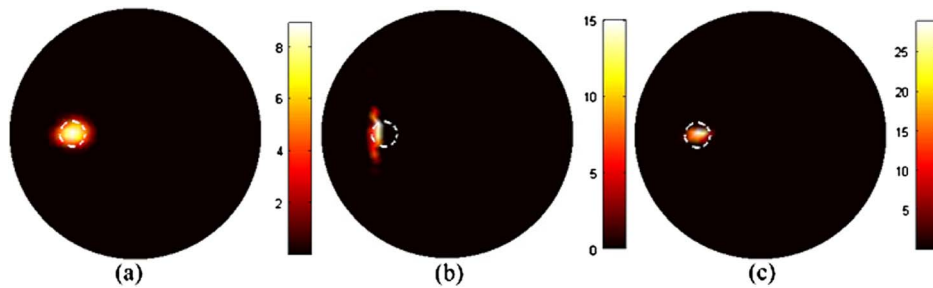


Fig. 2. (Color online) (a), (b), and (c) are the reconstructed results with l_2 , l_1 , and SBRTV regularizations, respectively, in the case of a single source for noiseless data. The white circles denote the real sources.

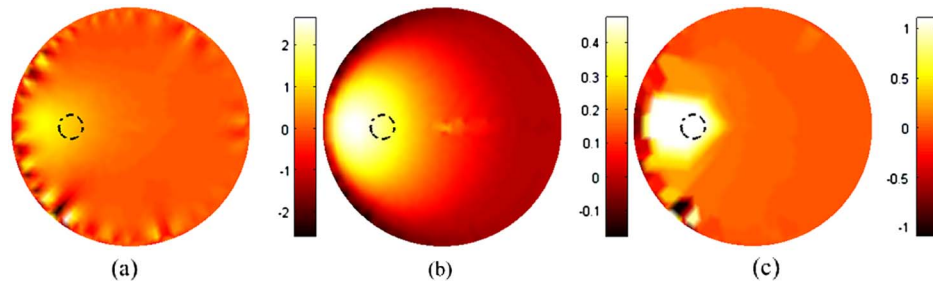


Fig. 3. (Color online) Reconstructed images without a nonnegativity constraint. (a), (b), and (c) are the results with l_2 , l_1 , and SBRTV regularizations, respectively. The black circles denote the real sources.

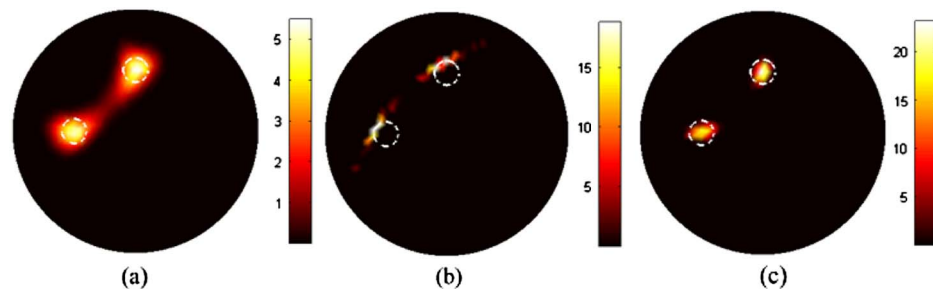


Fig. 4. (Color online) Reconstructed images with different regularization methods in the case of the two sources for noiseless data. (a) l_2 , (b) l_1 , and (c) SBRTV regularizations. The white circles represent the actual sources.

Table 3. Reconstruction Results Using l_2 , l_1 , and SBRTV Regularization Methods in Case of Two Sources

Regularization method	Regularization parameter	No. source	Reconstructed position error	Reconstructed density error	MSE
l_2	4.56×10^{-5}	No. 1	0.54 mm	83.77%	14.26
		No. 2	0.15 mm	86.44%	
l_1	2.36×10^{-4}	No. 1	1.05 mm	39.35%	17.38
		No. 2	0.99 mm	46.26%	
SBRTV	1.15×10^{-7}	No. 1	0.21 mm	25.35%	9.65
		No. 2	0.15 mm	48.38%	

reconstruction algorithm can be enhanced and an accurate solution for the source distribution can be calculated. To further demonstrate the necessity of a nonnegativity constraint, simulations without a nonnegativity constraint were performed. The simulated data and parameter setting used in the case were the same as those of case 1. Figure 3(c) is the result with the SBRTV regularization but without a nonnegativity constraint. For comparison purposes, reconstructed images using l_2 and l_1 regularizations are also shown in Fig. 3. In contrast to Fig. 2, we can see that there is a need to apply a nonnegativity constraint for BLT reconstructions.

3. Case 3: Multiple Bioluminescent Sources

In the test, reconstructions with multiple bioluminescent sources were performed. First, the experiment with two bioluminescent sources (source 1 and source 2 in Fig. 1) was used to test the performance of the proposed algorithm. The two sources had a different source density and were centered at (−5 mm, 0 mm) and (0 mm, 5 mm), respectively. The radii of the sources were 1 mm as in the previous simulation. In Fig. 4, we show the results with l_2 , l_1 , and SBRTV regularizations. Quantitative results were compiled in Table 3. As in the previous example, l_2 reconstruction [Fig. 4(a)] suffers from the low

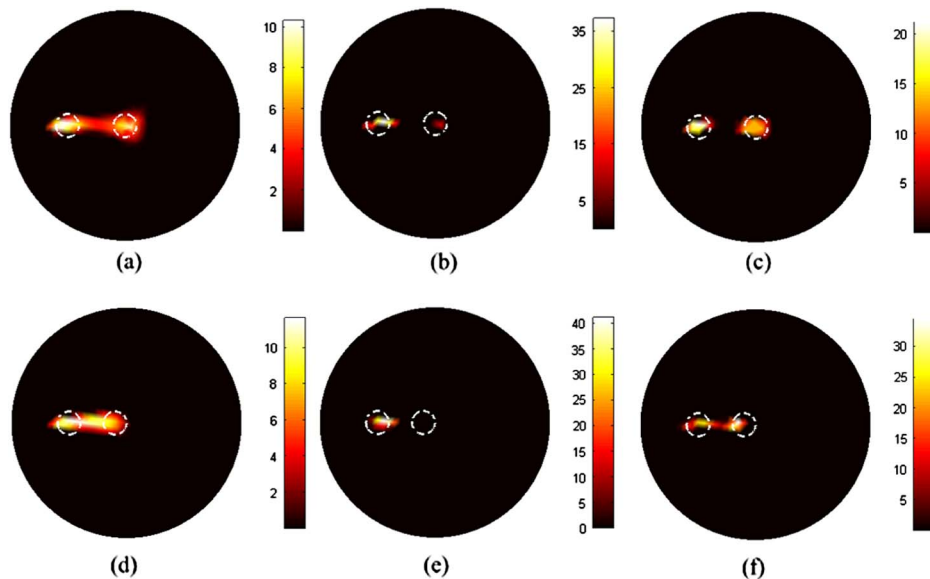


Fig. 5. (Color online) Reconstructed images with different edge-to-edge distances. The edge-to-edge distance of the first row is 3 mm, and the second row is 2 mm. The first column shows the images reconstructed with l_2 regularizations, and the middle and right columns are the images using l_1 and SBRTV regularizations, respectively. The white circles represent the actual sources.

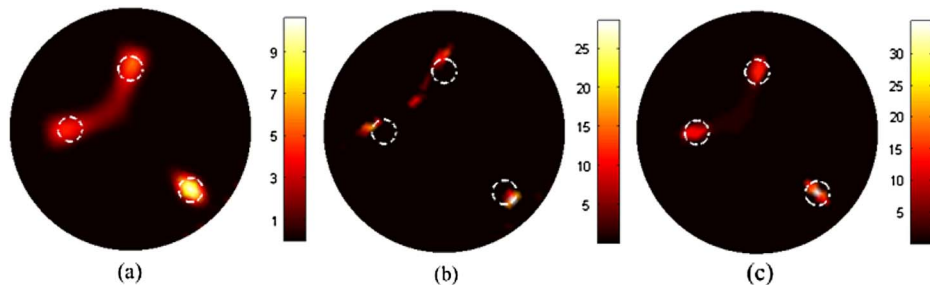


Fig. 6. (Color online) Comparison of different regularizations in case of three sources with noiseless data. (a), (b), and (c) are reconstruction results with l_2 , l_1 , and SBRTV regularizations, respectively. The white circles represent the actual sources.

Table 4. Reconstruction Results Using l_2 , l_1 , and SBRTV Regularization Methods in Case of Three Sources with Noiseless Data

Regularization method	Regularization parameter	No. source	Reconstructed position error	Reconstructed density error	MSE
l_2	4.56×10^{-5}	No. 1	0.54 mm	85.81%	21.31
		No. 2	0.14 mm	84.5%	
		No. 3	0.07 mm	67.91%	
l_1	2.36×10^{-4}	No. 1	1.05 mm	44.74%	27.61
		No. 2	1.13 mm	67.24%	
		No. 3	0.93 mm	13.36%	
SBRTV	1.15×10^{-7}	No. 1	0.21 mm	49.65%	18.43
		No. 2	0.15 mm	45.03%	
		No. 3	0.21 mm	5.39%	

resolution, and the sources cannot be distinguished. For l_1 reconstruction [Fig. 4(b)], although the sources can be distinguished, the source distributions are still sparsified. In contrast, the SBRTV regularization has a lower MSE and shows a good image quality. Meanwhile, the sources can be well distinguished.

To further evaluate our algorithm, BLT reconstructions were performed when source 1 and source 4 existed. In this case, the edge-to-edge distance of the two sources is 3 mm. Figures 5(a)–5(c) exhibit reconstructed images using different regularizations. The results are similar to those of Fig. 4. Next, source

4 was moved toward source 1, and the edge-to-edge distance of the two sources became 2 mm. The corresponding results are shown in Figs. 5(e) and 5(f). From the figures, we can see that the reconstructed sources are oversmoothed for l_2 regularization. While l_1 regularization significantly sparsifies the source distribution and produces high intensity. This leads to reconstruction failure for localization of the source 4. However, the SBRTV regularization again gives accurate source distribution.

Furthermore, three bioluminescent sources (source 1, source 2, and source 3) are placed as shown

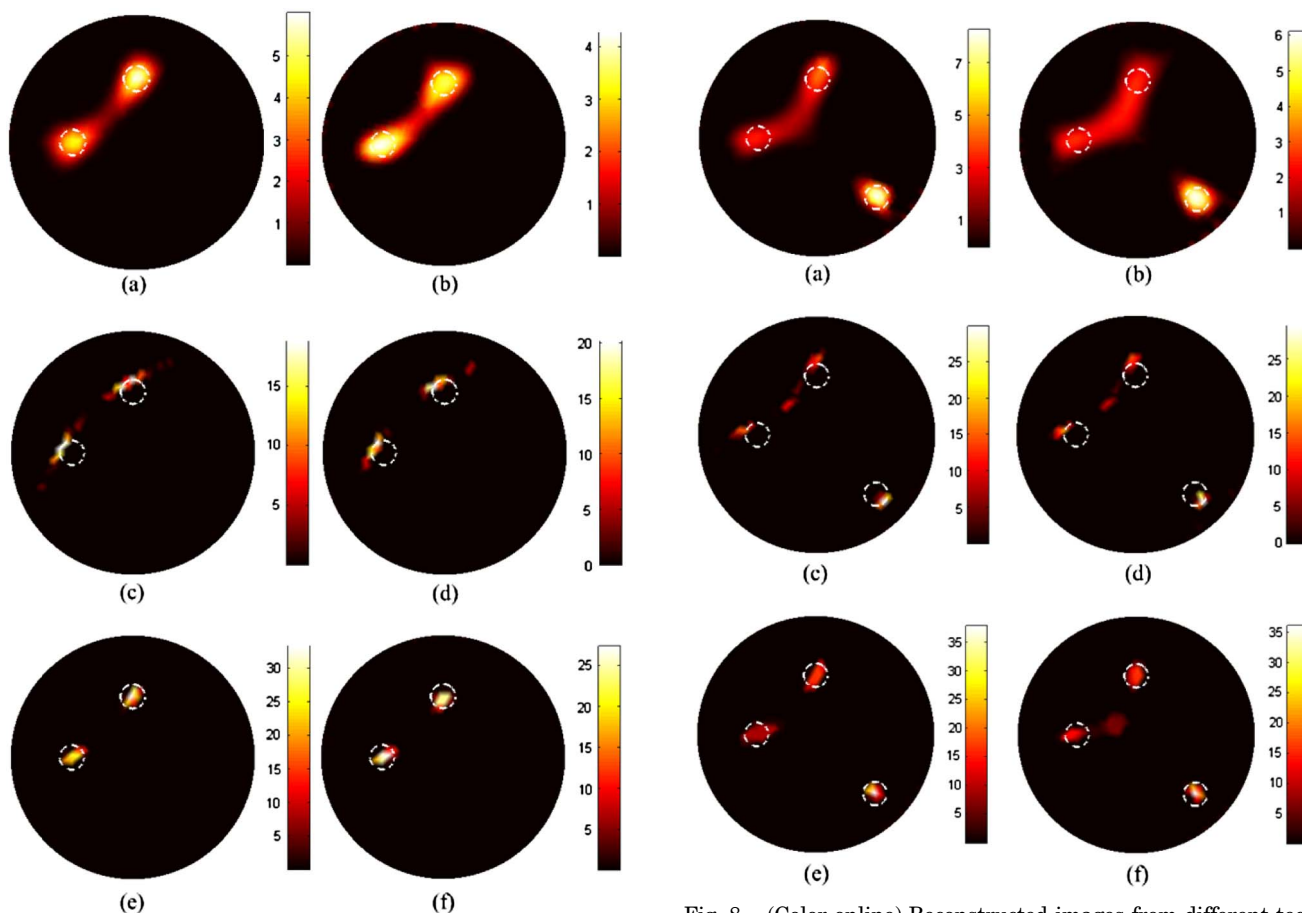


Fig. 7. (Color online) Reconstructed images with 10% (the left column) and 30% (the right column) noisy data. The first and middle rows use l_2 and l_1 regularizations, while the last row shows the results with the SBRTV regularization. The white circles represent the actual sources.

Fig. 8. (Color online) Reconstructed images from different techniques with simulated data having 5% (the left column) and 10% (the right column) noise. The first and middle rows show the reconstruction results with l_2 and l_1 regularizations, while the last row shows the results with SBRTV regularization. The white circles represent the actual sources.

in Fig. 1. Figure 6 and Table 4 show the reconstructed BLT images and quantitative results for the three sources, respectively. Similar to the above cases, the better results were obtained again by the SBRTV regularization.

4. Case 4: Noise Analysis

It is well known that all regularization methods are able to suppress noise with different degrees. In order to analyze the performance of the SBRTV regularization, different levels of Gaussian noise were added to the boundary measurements. Figure 7 illustrates the reconstructed BLT images with different regularization methods and different levels of noisy data. The images [Figs. 7(a) and 7(b)] of l_2 regularization are oversmoothed and demonstrate low spatial resolution in the cases of noisy data, and sources are not distinguished. l_1 regularization results in sparse source distribution, and artifacts exist at both 10% and 30% levels. However, the two sources are distinguished. In contrast, the SBRTV regularization is able to suppress more noise than

l_2 and l_1 regularizations, but the reconstructed images decay as the noise increases.

The reconstructions for the three sources are shown in Fig. 8. As seen from the figure, SBRTV regularization can exhibit better image quality than the images obtained using l_2 and l_1 regularizations, even though artifacts still appear, which can be removed by choosing a proper threshold.

5. Case 5: Different Numbers of Measurements

In this part, we reported the reconstruction quality of different images using different numbers of measurements for three types of regularization. 3% Gaussian noise was added to the simulation data, and results are indicated in Fig. 9. From the figure, we find that when reducing the number of measurements, the reconstruction quality is gradually degraded in all cases. Otherwise, the images that are best reconstructed use our algorithm, which shows that the SBRTV regularization is efficient in recovering bioluminescent images with fewer measurements. These numerical results also suggest

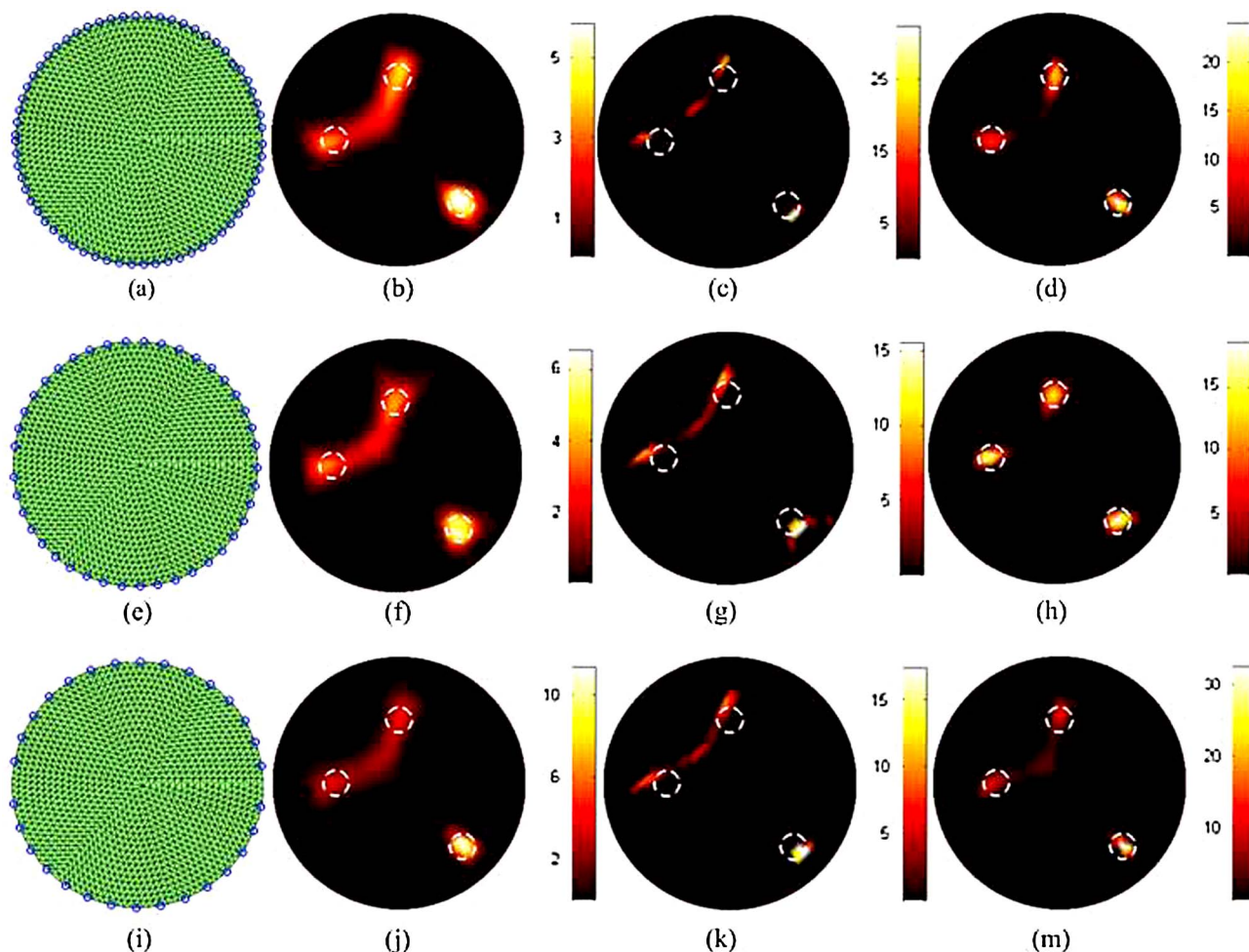


Fig. 9. (Color online) The left column is the configuration with detectors, and the small circles indicate the detector locations. The number of detectors for each wavelength from the top to bottom is 63, 41, and 30 respectively. The middle two columns and the last column are the results with l_2 , l_1 , and SBRTV regularizations with 3% Gaussian noise added to the simulated data. The white circles represent the actual sources.

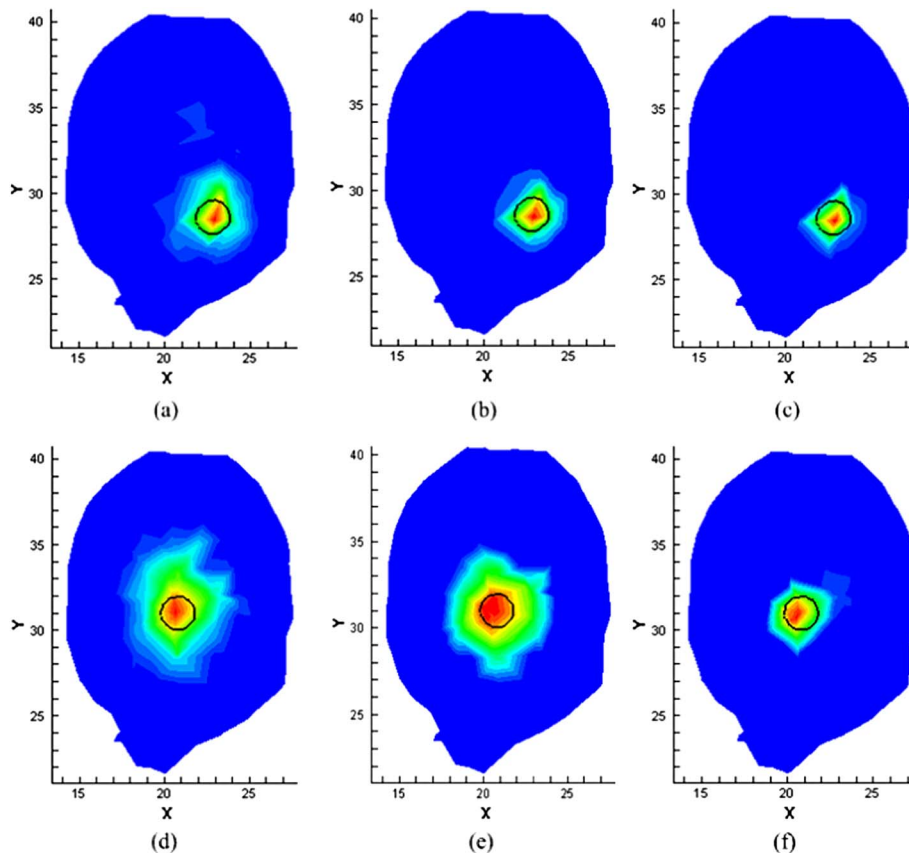


Fig. 10. (Color online) 3D reconstruction results for a cross-section of the 3D model at $z = 12.5$ mm. (a)–(c) are the corresponding results with l_2 , l_1 , and TV regularization methods, respectively, when the source locates at (22.8, 28.6, 12.5) mm. (d)–(f) are the corresponding results with l_2 , l_1 , and SBRTV regularization methods, respectively, when the source locates at (20.8, 30.96, 12.5) mm. The axes (left and bottom) illustrate the spatial scale in millimeters, and the black circles denote the actual sources.

that the reconstruction performance is dependent upon the number of measurements.

B. 3D Simulation Results

In order to test the SBRTV based BLT reconstruction algorithm, a numerical mouse model derived from CT images was used. The mouse model consisted of five different tissues with different optical properties. More detailed information about the mouse

model and the optical properties of tissues can be obtained elsewhere in [35]. Synthetic measurement data in three spectral bands ([600, 750] nm in 50 nm steps) were produced by a Monte Carlo based molecular optical simulation environment (MOSE) [36]. For BLT reconstructions, the mouse model was discretized into an unstructured mesh with 2579 nodes, 13 200 tetrahedron element, and 697 boundary measurement points. A spherical solid

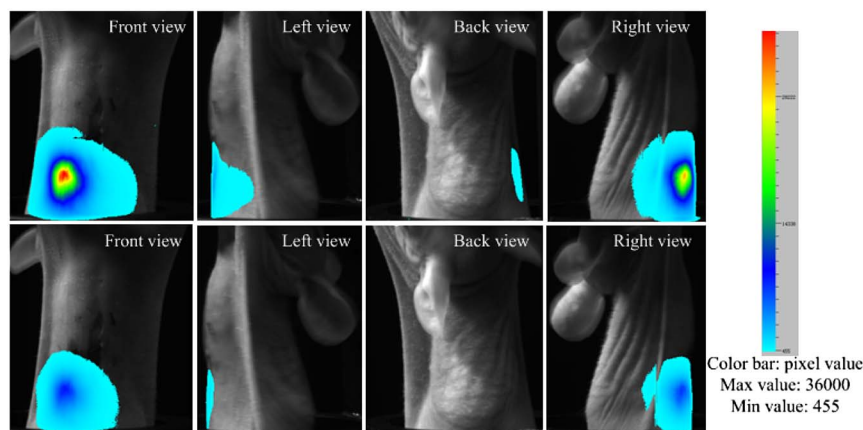


Fig. 11. (Color online) Bioluminescent images overlaid on the corresponding white light images of the mouse. The top and the bottom rows are images of [650–700] nm and [700–750] nm, respectively.

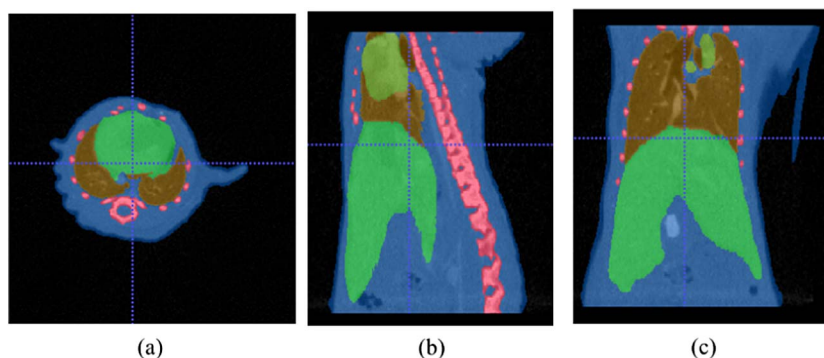


Fig. 12. (Color online) (a) Transverse view of the mouse. (b) and (c) are the corresponding coronal view and sagittal view, respectively. Different colors correspond to different tissue types (royal blue, muscle; saddle brown, lungs; red, bones; lime green, liver; yellow green, heart).

Table 5. Optical Parameters for Different Bands. (Unit: mm^{-1})

Wavelength	650–700 nm		700–760 nm	
	μ_a	μ'_s	μ_a	μ'_s
Muscle	0.0771	0.4128	0.0396	0.3373
Heart	0.0521	0.9446	0.0282	0.8529
Lung	0.1741	2.1574	0.0899	2.0775
Liver	0.3129	0.6680	0.1646	0.6198
Bone	0.0540	2.4441	0.0280	2.2005

source with a radius of 1.0 mm was placed in different depths (about 4.1 mm and 6.2 mm) with coordinates of (22.8, 28.6, 12.5) mm and (20.8, 30.98, 12.5) mm, respectively. Figure 10 illustrates the corresponding reconstruction results using three regularization methods. From Fig. 10, we can see that the source positions are well localized. And the central positions of the reconstructed source for different depths utilizing three regularization methods were same and were (23.48, 28.55, 12.04) mm and (20.37, 31.05, 12.95) mm, respectively. However, when the l_2 regularization was used, the reconstructed images were oversmoothed, and the worse image quality was obtained. Furthermore, it is observed that the l_1 regularization can improve BLT reconstruction quality compared with the l_2 regularization. Also, it is observed that the performance of

SBRTV regularization outperforms other regularizations such as l_2 and l_1 regularizations.

C. In vivo Experiment

In this subsection, we gave an *in vivo* heterogeneous mouse example to further demonstrate the effectiveness of the SBRTV regularization. A dual-modality optical/micro-CT system was used to acquire the bioluminescent data and the 3D CT data [24]. To imitate the bioluminescent source, a luminescent bead was created in our lab, and its wavelength spectrum was similar to that of firefly luciferase. For bioluminescent image acquisition, a multiview noncontact detection scheme was used with a highly sensitive CCD camera (VersArray, Princeton Instruments, Trenton, New Jersey) coupled with a Micro-Nikkor 55 mm $f/2.8$ lens. To measure the bioluminescent signal, a group of glass cutoff filters was placed in front of the CCD. The whole setup was placed in a totally dark environment to reduce light leaking.

For each wavelength, four views (front, right, back, and left views) were acquired. After image processing, bioluminescent images at two wavelengths ([650, 700] nm, and [700, 750] nm) were obtained. Figure 11 shows the acquired images for the two wavelengths. Prior to 3D reconstruction, each 2D image needed to be mapped onto the surface of the mouse, and all data were normalized to their

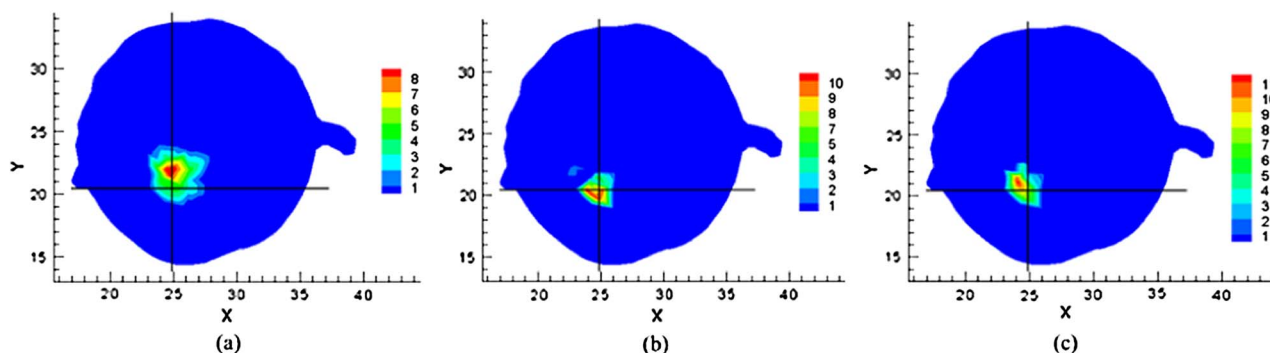


Fig. 13. (Color online) *In vivo* reconstruction results. (a), (b), and (c) are l_2 , l_1 , and SBRTV regularizations, respectively. Only the slice through the actual source's center is shown and the crossing white lines denote the actual source central position. The axes (left and bottom) illustrate the spatial scale in millimeters.

Table 6. Quantitative Results for Different Regularization Methods

	l_2	l_1	SBRTV
Iteration number	19	22063	9
Time (seconds)	113	437	2084
λ	4.7×10^{-5}	1.6×10^{-3}	4.7×10^{-5}
Reconstructed error (mm)	1.66	0.84	0.84

maximum light intensity value. After BLT data acquisition, the mouse was scanned by a Micro-CT system. Afterwards, 3D CT data were manually segmented into five different tissues, including lungs, bone, heart, liver and muscle, as shown in Fig. 12. With respect to the photon distribution, about 3/5 of the whole mouse was used for mesh generation. The mesh contained 19 088 tetrahedral elements and 3665 vertex nodes with 763 nodes on the surface. Optical properties for tissues at each node of the tetrahedral volume were assigned according to the formulations in [37]. Table 5 shows the optical property parameters used in the reconstruction. The center position of the bioluminescent source was (24.89, 20.4, 7.88) mm, which was determined by CT data. Different regularization methods were then performed to reconstruct the bioluminescent source, and results were presented in Fig. 13. Quantitative information is summarized in Table 6. The SBRTV regularization was terminated after nine outer loops. The convergence speed of the SBRTV regularization can be found in Fig. 14, where we have plotted the objective function calculated by Eq. (9) versus the iteration number. From the figure, we can see that the SBRTV regularization converges quickly. The center position of the recovered source for the SBRTV technique is (24.47, 20.27, 7.17) mm, and the offset to the center of the true source is 0.84 mm. The reconstructed source position for l_1 is the same as for the SBRTV, but an artifact exists. The position of the reconstructed source with the l_2 regularizer is (24.42, 21.73, 8.75) mm, and the offset is 1.66 mm. Comparing these figures, we can conclude that the

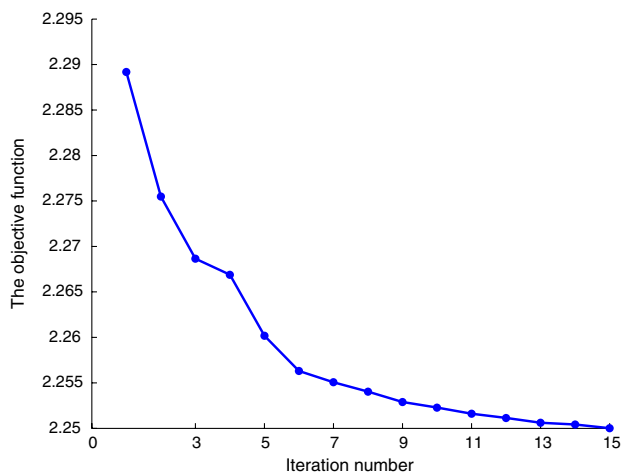


Fig. 14. (Color online) The value of objective function versus outer iteration number for SBRTV regularization.

SBRTV regularization can improve the quality of the BLT reconstruction.

4. Conclusion

It is well known that the reconstruction of BLT is ill-posed and regularization techniques are essential to recover the bioluminescent source. However, the quality of reconstructed images largely depends on the choice of a regularizer. In this paper, we investigated SBRTV regularization with application to BLT including single/multiple source(s) and noisy data. Moreover, bioluminescent sources reconstructed from a very small number of measurements were also analyzed. For 2D simulations, the bioluminescent sources could be reconstructed with good accuracy for the location; see Figs. 2, 4–10, and 13. The mean position errors for l_2 , l_1 , and SBRTV regularizations in Tables 2–4 are 0.275, 1.01, and 0.19 mm, respectively. The variances for l_2 , l_1 , and SBRTV regularizations are 0.0411 mm^2 , 0.0077 mm^2 , and $9.6e-4 \text{ mm}^2$, respectively. From the quantitative results, we can conclude that SBRTV regularization provides better image quality compared with l_2 and l_1 regularizations. 3D simulation and *in vivo* mouse experiments further evaluated the performance of SBRTV regularization.

An open issue is with regard to the computation time for the SBRTV regularization. The SBRTV regularization is very time-consuming compared with l_2 and l_1 regularizations. As an example, on a desktop computer with Intel Core 2 Quad Q9550 2.83 GHz CPU with TV regularization, computation takes about 30 min in a 3D mouse in contrast of minutes in 2D on MATLAB as the simulation platform. On the other hand, the computational time for l_2/l_1 regularization is around one twentieth/fifth of that of the SBRTV regularization. This is because solving TV regularization through the split Bregman method brings extra cost and is needed to compute two subproblems (step 1 and step 2) by iteratively minimizing. Note that step 2 is computed by a shrinkage operator, which is extremely fast and requires only a few operations per element of u_{k+1} . Our *in vivo* example also agrees with the above analysis. The computational time for step 1 is about 2069 s, and for step 2 it is about 0.39 s, and the remaining time is for data reading and other tasks. Therefore, the computational time for the SBRTV regularization is nearly equivalent of solving a subproblem (step 1). Step 1 is a common l_2 problem, and it can be solved by many fast optimization algorithms, such as the limited-memory Broyden–Fletcher–Goldfarb–Shanno (L-BFGS) algorithm, to improve the computational efficiency.

On the other hand, performing the SBRTV regularization requires large amounts of computer memory because an additional matrix D needs to be constructed, as compared with the other two regularization methods, and its size is very large, especially for 3D mouse reconstruction; for example, the size of D was (88216×3665) in the mouse experiment.

A further speed-up of the method is possible by parallelization.

Note that we are not declaring that we will propose a faster algorithm than in the existing methods, but we are proposing a simple and effective algorithm to solve TV regularization to improve the reconstruction quality for BLT.

This paper is supported by the National Basic Research Program of China (973 Program) under Grant No. 2011CB707700, the Knowledge Innovation Project of the Chinese Academy of Sciences under Grant No. KGCX2-YW-907, the National Natural Science Foundation of China under Grant Nos. 30970780, 81000624, 81027002, 81071205, the Science and Technology Key Project of Beijing Municipal Education Commission under Grant No. KZ200910005005, the Doctoral Fund of the Ministry of Education of China under Grant No. 20091103110005, and the Scientific Research Fund of Beijing University of Technology under Grant No. X0002012201101.

†These authors contributed equally to this work.

References

1. J. K. Willmann, N. van Bruggen, L. M. Dinkelborg, and S. S. Gambhir, "Molecular imaging in drug development," *Nat. Rev. Drug Discov.* **7**, 591–607 (2008).
2. G. C. Kagadis, G. Loudos, K. Katsanos, S. G. Langer, and G. C. Nikiforidis, "In vivo small animal imaging: current status and future prospects," *Med. Phys.* **37**, 6421–6442 (2010).
3. X. Ma, J. Tian, X. Yang, C. Qin, S. Zhu, and Z. Xue, "Research on liver tumor proliferation and angiogenesis based on multi-modality molecular imaging," *Acta Biophys. Sin.* **27**, 355–364 (2011).
4. C. H. Contag and M. H. Bachmann, "Advances in in vivo bioluminescence imaging of gene expression," *Annu. Rev. Biomed. Eng.* **4**, 235–260 (2002).
5. D. Kepshire, N. Mincu, M. Hutchins, J. Gruber, H. Dehghani, J. Hynarowski, F. Leblond, M. Khayat, and B. W. Pogue, "A microcomputed tomography guided fluorescence tomography system for small animal molecular imaging," *Rev. Sci. Instrum.* **80**, 043701 (2009).
6. H. Gao and H. Zhao, "Multilevel bioluminescence tomography based on radiative transfer equation Part I: l1 regularization," *Opt. Express* **18**, 1854–1871 (2010).
7. H. Gao and H. Zhao, "Multilevel bioluminescence tomography based on radiative transfer equation Part 2: total variation and l1 data fidelity," *Opt. Express* **18**, 2894–2912 (2010).
8. H. Dehghani, S. C. Davis, S. Jiang, B. W. Pogue, K. D. Paulsen, and M. S. Patterson, "Spectrally resolved bioluminescence optical tomography," *Opt. Lett.* **31**, 365–367 (2006).
9. J. Feng, K. Jia, G. Yan, S. Zhu, Y. Lv, and J. Tian, "An optimal permissible source region strategy for multispectral bioluminescence tomography," *Opt. Express* **16**, 15640–15654 (2008).
10. Y. Lv, J. Tian, W. Cong, G. Wang, W. Yang, C. Qin, and M. Xu, "Spectrally resolved bioluminescence tomography with adaptive finite element analysis: methodology and simulation," *Phys. Med. Biol.* **52**, 4497–4512 (2007).
11. Y. Lv, J. Tian, W. Cong, G. Wang, J. Luo, W. Yang, and H. Li, "A multilevel adaptive finite element algorithm for bioluminescence tomography," *Opt. Express* **14**, 8211–8223 (2006).
12. Y. Lu, B. Zhu, H. Shen, J. C. Rasmussen, G. Wang, and E. M. Sevick-Muraca, "A parallel adaptive finite element simplified spherical harmonics approximation solver for frequency domain fluorescence molecular imaging," *Phys. Med. Biol.* **55**, 4625–4645 (2010).
13. A. D. Klose, B. J. Beattie, H. Dehghani, L. Vider, C. Le, V. Ponomarev, and R. Blasberg, "In vivo bioluminescence tomography with a blocking-off finite-difference SP₃ method and MRI/CT coregistration," *Med. Phys.* **37**, 329–338 (2010).
14. K. Liu, J. Tian, C. Qin, X. Yang, S. Zhu, D. Han, and P. Wu, "Tomographic bioluminescence imaging reconstruction via a dynamically sparse regularized global method in mouse models," *J. Biomed. Opt.* **16**, 046016 (2011).
15. L. Rudin, S. Osher, and E. Fatemi, "Nonlinear total variation based noise removal algorithms," *Physica D* **60**, 259–268 (1992).
16. A. Chambolle, "An algorithm for total variation minimization and applications," *J. Math. Imaging Vision* **20**, 89–97 (2004).
17. T. Chan and C. K. Wong, "Total variation blind deconvolution," *IEEE Trans. Image Process.* **7**, 370–375 (1998).
18. K. D. Paulsen and H. Jiang, "Enhanced frequency-domain optical image reconstruction in tissues through total-variation minimization," *Appl. Opt.* **35**, 3447–3458 (1996).
19. L. Yao and H. Jiang, "Enhancing finite element based photoacoustic tomography using total-variation minimization," *Appl. Opt.* **50**, 5031–5041 (2011).
20. L. Yao and H. Jiang, "Photoacoustic image reconstruction from few-detector and limited-angle data," *Biomed. Opt. Express* **2**, 2649–2654 (2011).
21. S. Ahn, A. J. Chaudhari, F. Darvas, C. A. Bouman, and R. M. Leahy, "Fast iterative image reconstruction methods for fully 3D multispectral bioluminescence tomography," *Phys. Med. Biol.* **53**, 3921–3942 (2008).
22. A. J. Chaudhari, F. Darvas, J. R. Bading, R. A. Moats, P. S. Conti, D. J. Smith, S. R. Cherry, and R. M. Leahy, "Hyperspectral and multispectral bioluminescence optical tomography for small animal imaging," *Phys. Med. Biol.* **50**, 5421–5441 (2005).
23. H. Dehghani, S. C. Davis, and B. W. Pogue, "Spectrally resolved bioluminescence tomography using the reciprocity approach," *Med. Phys.* **35**, 4863–4871 (2008).
24. J. Feng, K. Jia, C. Qin, G. Yan, X. Zhang, J. Liu, and J. Tian, "3D bioluminescence tomography based on Bayesian approach," *Opt. Express* **17**, 16834–16848 (2009).
25. G. Wang, Y. Li, and M. Jiang, "Uniqueness theorems in bioluminescence tomography," *Med. Phys.* **31**, 2289–2299 (2004).
26. S. Osher, M. Burger, D. Glodfarb, J. Xu, and W. Yin, "An iterative regularization method for total variation based image restoration," *Multiscale Model. Simul.* **4**, 460–489 (2005).
27. T. Goldstein and S. Osher, "The split Bregman method for L1-regularized problems," *SIAM J. Imaging Sci.* **2**, 323–343 (2009).
28. T. Goldstein, X. Bresson, and S. Osher, "Geometric applications of the split Bregman method: segmentation and surface reconstruction," *J. Sci. Comput.* **45**, 272–293 (2010).
29. J. Cai, S. Osher, and Z. Shen, "Linearized Bregman iterations for compressed sensing," *Math. Comput.* **78**, 1515–1536 (2009).
30. J. Cai, S. Osher, and Z. Shen, "Convergence of the linearized Bregman iteration for l1-norm minimization," *Math. Comput.* **78**, 2127–2136 (2009).
31. W. Yin, S. Osher, D. Goldfarb, and J. Darbon, "Bregman iterative algorithms for l1-minimization with applications to compressed sensing," *SIAM J. Imaging Sci.* **1**, 143–168 (2008).
32. J. Feng, C. Qin, K. Jia, D. Han, K. Liu, S. Zhu, X. Yang, and J. Tian, "An adaptive regularization parameter choice strategy for multi-spectral bioluminescence tomography," *Med. Phys.* **38**, 5933–5944 (2011).
33. T. F. Coleman and Y. Li, "A reflective newton method for minimizing a quadratic function subject to bounds on some of the variables," *SIAM J. Optim.* **6**, 1040–1058 (1996).
34. M. T. Figueiredo, R. D. Nowak, and S. J. Wright, "Gradient projection for sparse reconstruction: application to compressed sensing and other inverse problems," *IEEE J. Sel. Top. Signal Process.* **1**, 586–597 (2007).
35. J. Feng, K. Jia, C. Qin, S. Zhu, X. Yang, and J. Tian, "Sparse Bayesian reconstruction method for multispectral bioluminescence tomography," *Chin. Opt. Lett.* **8**, 1010–1014 (2010).
36. H. Li, J. Tian, F. Zhu, W. Cong, L. V. Wang, E. A. Hoffman, and G. Wang, "A mouse optical simulation environment (MOSE) to investigate bioluminescent phenomena in the living mouse with Monte Carlo method," *Acad. Radiol.* **11**, 1029–1038 (2004).
37. G. Alexandrakakis, F. R. Rannou, and A. F. Chatziioannou, "Tomographic bioluminescence imaging by use of a combined optical-PET (OPET) system: a computer simulation feasibility study," *Phys. Med. Biol.* **50**, 4225–4241 (2005).